ACS OMEGA

http://pubs.acs.org/journal/acsodf

Article

PANI@UiO-66 and PANI@UiO-66-NH_2 Polymer-MOF Hybrid Composites as Tunable Semiconducting Materials

Jordan Shanahan,[§] Daniel S. Kissel,[*,§] and Eirin Sullivan[§]

Cite This: *ACS Omega* 2020, 5, 6395−6404

Read Online

ACCESS | Metrics & More | Article Recommendations | Supporting Information

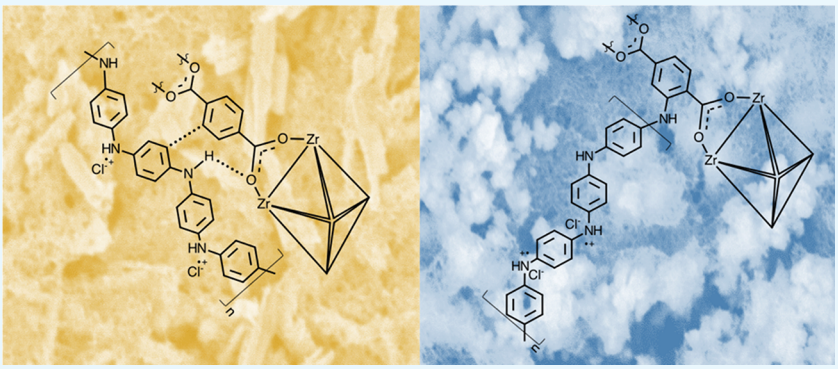

ABSTRACT: This investigation explores optimum synthetic conditions for novel polymer-metal organic framework hybrid composites composed of Zr-terephthalate-based MOF UiO-66 and conductive polyaniline (PANI) nanofibers in an effort to optimize conductivity while minimizing MOF structural deformation. Successful syntheses of self-assembled PANI nanofibers in PANI@UiO-66 and PANI@UiO-66-NH_2 composites were confirmed using scanning electron microscopy, infrared spectroscopy, and powder X-ray diffraction. The polymer-MOF composites show different bonding synergies to the PANI nanofibers depending on the organic linker used. Electronic properties of the post-synthetically modified PANI@UiO-66 and PANI@UiO-66-NH_2 were investigated using UV−vis diffuse reflectance spectroscopy. Sheet resistivity of the self-assembled polymer-MOF composites was determined under an inert atmosphere at room temperature using four-point probe measurements to confirm tunable semiconductivity ranging from 40 to 2 mS/sq. Furthermore, the effects of aniline oxidation on the crystallinity and coordination of UiO-66 and UiO-66-NH_2 were determined through analysis of these results.

1. INTRODUCTION

Metal−organic frameworks (MOFs) have emerged as highly versatile materials studied for numerous applications including gas adsorption,[1,2] drug delivery,[3] and catalysis[4,5] among others. MOFs feature inorganic metal ion nodes linked together through easily tailored organic ligands, which provide a high degree of tunability and large specific surface areas. These traits are also useful for designing thin-film electrode materials for capacitors or electrocatalytic electrodes; however, there has been little research on MOFs in electronic-based applications because of limited charge transport capabilities. Isolation of the inorganic nodes and the inability of constrained phenyl linkers to π stack limits the desirable delocalized charge carrier capabilities found in their pure metal oxide counterparts.[6,7] Although, there are examples of MOFs reported in literature that show conducting and semiconducting behaviors utilizing 2-dimensional stacking structures.[8,9] There have also been examples of highly porous conductive MOFs created through guest molecule loading, which act as mediators to achieve a Schottky junction between metal clusters.[10] In the former case, these highly desirable structures come at the cost of long term environmental and chemical stabilities, and in the latter case, the reagent materials used are often quite expensive limiting their practicality. Ideally, a semiconducting MOF material would be chemically robust and affordable, which would be attractive for use in several electronic-based applications including dye-sensitized solar cells, electrocatalytic cells, and electrochemical sensing amongst others.

Interestingly, MOFs composed of tetravalent group IV metal ions and carboxylate ligands possess some of the strongest coordination bonds reported in literature, significantly increasing research interests in these materials over the last ten years.[11−13] More specifically, zirconium MOFs using the octahedral $[Zr_6O_4(OH)_4]^{12+}$ secondary building unit (SBU)

Received: November 11, 2019
Accepted: February 28, 2020
Published: March 17, 2020

https://dx.doi.org/10.1021/acsomega.9b03834
ACS Omega 2020, 5, 6395−6404

coordinated with linear ligands possess additional degrees of tunability without the loss of crystallinity and superb chemical robustness.[14,15] The most basic motif utilizes terephthalic acid (TPA) ligands as linkers, known as UiO-66, and has shown unprecedented thermal stability. UiO-66 has proved stable in most polar solvents and acidic conditions, and it has thermal stability reported up to 500 °C.[14,15] Regarding catalytic and photocatalytic systems, modified UiO-66 MOFs have shown potential as molecular photocatalysts for a variety of reactions including water splitting.[5,16,17] Simple pre- and postsynthetic modifications to the TPA ligands can extend the optical bandgap of the MOF considerably. For example, an amine functionality introduced presynthetically into the TPA ligand extends the bandgap of UiO-66 by more than 1 eV.[18,19] Unfortunately, due to the localization of charge carriers, Zr-based MOFs have not been attractive solutions for use in electrochemical and photoelectrochemical cells.

The introduction of a novel conducting mediator could be used to impart true semiconducting behavior unto Zr-based MOFs. This work therefore seeks to provide UiO-66 and conjugate UiO-66-NH_2 with a stable, low-cost mode of electron transport directly through the in situ synthesis of a conductive organic polymer functionalized onto the MOF. Polyaniline (PANI) was chosen as a mediator for its favorable electrostatic interactions between the organic terephthalic linker (TPA) and the aniline precursor. Furthermore, PANI is an extensively studied conductive organic polymer due to its simple and tunable synthesis and high environmental stability.[20,21] It has been shown to possess relatively high conducting capability in its emeraldine salt state from a combination of an extended π network and plasmonic effects caused by radical cation amines coupled to anions.[22] PANI typically forms thin nanofibrous films through π stacking of aniline subunits upon evaporation of solvent. These nanofibers were perceived to bridge Zr-based MOF particles creating a cohesive polymer-MOF hybrid composite network.[25] This ensures a simple, scalable film preparation that could be used as a novel electrode material.

Polymer-MOF hybrids have only recently appeared in literature and are thought to combine the highly attractive features of both materials for applications in enhancing the surface area and control of polymer chain functionality. Wang et al. demonstrated the specific PANI-UiO-66 electrostatic relationship on a nanoscopic scale for applications in photothermal treatment.[26] Their finding also showed increased chemical stability of the polymer in the composite material. A separate report from this group highlighted its potential as an electrochemical sensor and supercapacitor.[35,36,40] An even more recent work discusses the possible use of a polymer-MOF material as supports in photocatalytic systems, but to our knowledge, no work has been done that investigates the effects of oxidative stress and high PANI concentration on structural integrity and conductive capability.[39] The PANI@UiO-66 composites used in this study not only exhibit higher relative PANI concentrations and self-assembled films compared to the above sources but also feature direct comparison of TPA ligands that contain different functionalities. In the case of the conjugate UiO-66-NH_2, an amine moiety on the TPA linker was chosen to impart the MOF with a synthetic route for covalently cross-linking with PANI. In addition to the clear similarity in structures of aniline and the 2-aminoterephthalate (ATPA), the derivative UiO-66-NH_2 has been shown to readily undergo postsynthetic modification to form new bonds.[23,24] The covalency with amine surface sites at relatively high-concentration ratios was perceived to provide PANI@UiO-66-NH_2 films with enhanced bulk polymer stability. This work demonstrates the bulk interaction in the PANI@UiO-66 and PANI@UiO-66-NH_2 comparing thermal and chemical stabilities and conductivity effects relative to the concentration of oxidant and aniline used. The implications of this work provide a simple synthetic pathway to induce tunable, low cost conductivity via PANI@MOF polymer hybrid films as well as investigate the effects of conventional polymer reaction conditions on the MOF structure.

2. EXPERIMENTAL SECTION

2.1. Materials. Zirconium (IV) chloride, purchased ACRO Chemistry (AR purity 97%), terephthalic acid, and 2-aminoterephthalic acid purchased from Sigma-Aldrich (AR purity <99%) were used as precursors for UiO-66 and UiO-66-NH_2. *N*,*N*-dimethylformamide (DMF), purchased from Fisher Scientific (AR purity <99%), was used as a complexing solvent. Ammonia peroxydisulfate (APS), purchased from Sigma-Aldrich (AR purity <98%) and aniline, purchased from Fisher Scientific (AR purity <99%), were used as precursors for PANI synthesis. All chemicals are analytical grades and were used without any further purification.

2.2. UiO-66 and UiO-66-NH_2 Syntheses. UiO-66 synthesis was completed as a one-pot synthesis in Teflon-lined reaction vessel based on a solvothermal synthesis reported by Shearer et al.[27] Zirconium (IV) chloride (1.98 mmol) and terephthalic acid (1.98 mmol) precursors were dissolved in 34 mL of DMF. An addition of 340 μL of concentrated hydrochloric acid moderator was then added to improve ligand solvent exchange. The solution was placed in a 120 °C oven and heated for 24 h. The resulting precipitate was washed three times with DMF, and once with methanol, before being collected by vacuum filtration. This process was repeated substituting 2-aminoterephthalic acid for terephthalic acid to create UiO-66-NH_2.

2.3. PANI Synthesis. PANI synthesis was adapted from a one-pot synthetic procedure reported by Li et al.[25] An ammonium peroxydisulfate precursor solution was created by dissolving APS (0.799 mmol) in 10 mL of 1 M hydrochloric acid. Aniline (306 mmol) was dissolved in a separate vial containing 10 mL of 1 M hydrochloric acid. The APS precursor solution was then rapidly added to the aniline precursor solution. The vial was shaken for approximately 30 s and then left undisturbed to polymerize for 24 h at room temperature. PANI was then centrifuged and washed three times with 1 M HCl to remove excess APS.[29]

2.4. PANI@UiO-66 Composite Synthesis. Two separate aniline and APS stock solutions were prepared according to the PANI synthesis. UiO-66 (or UiO-66-NH_2) was then added to three empty vials (0.03 g in each). Aniline stock solution was diluted in accordance with the desired mass ratios of aniline monomer to MOF (1:1, 2:1, and 3:1). Briefly, the three vials containing MOF were prepped by adding 0.974, 1.947, and 2.921 mL of the aniline stock solution. Equivalent volumes of APS stock solution were added to a separate set of vials. All solutions were diluted with 1 M HCl to 4 mL each and sonicated for 30 min to suspend the MOF uniformly in solution. An additional control trial exposed the fully concentrated APS stock solution to MOF to confirm retention of the framework. From this point, the standard PANI synthesis was followed via the rapid addition of APS solutions

https://dx.doi.org/10.1021/acsomega.9b03834
ACS Omega 2020, 5, 6395−6404

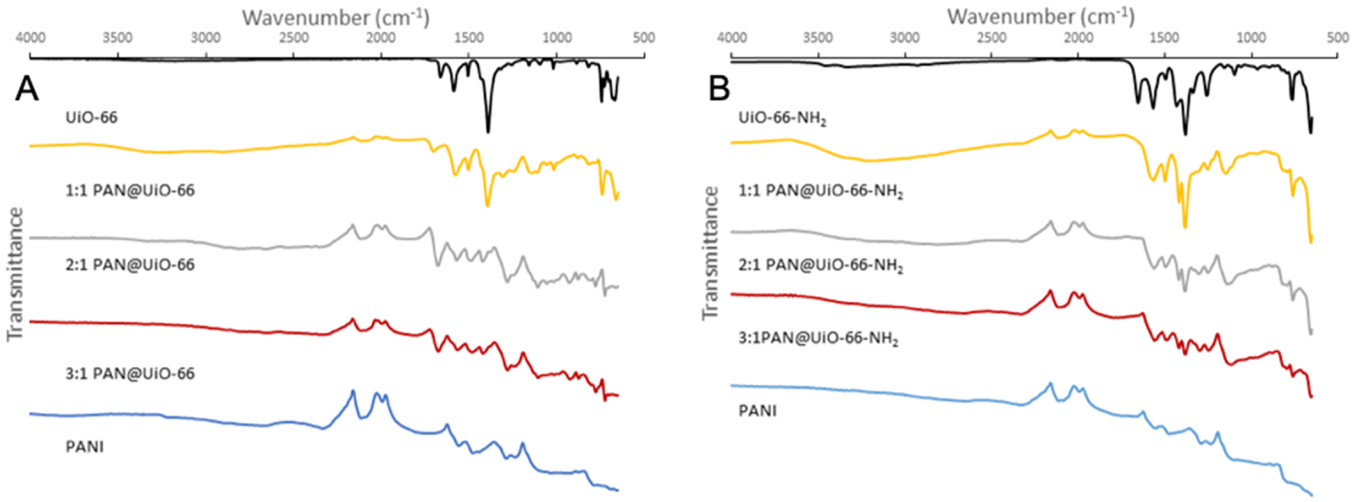

Figure 1. FT-IR of PANI@UiO-66 composites (A) and PANI@UiO-66-NH_2 composites (B).

to the corresponding aniline@MOF slurries. After full polymerization and washing, the composite slurries were drop casted on glass slides and formed polymer-MOF hybrid films through evaporation-assisted self-assembly of PANI nanofibers.

3. INSTRUMENTATION

Functional groups of the PANI@MOF composites were identified using Fourier transform infrared attenuated total resonance (FT-IR-ATR) spectroscopy on a CARY 630 FT-IR spectrometer. Powder X-ray diffraction (PXRD) data of the MOFs and PANI@MOF composites were collected on a Rigaku Miniflex 600 benchtop diffractometer using a Cu anode with Kα1 = 1.5406(5) Å and Kα2 = 1.5444(5) Å fitted with a Ni Kβ filter. Samples were analyzed between 2θ = 5−80° with a step size of 0.01 degrees and a scan speed of 0.2 degrees/min. Thermogravimetric analysis (TGA) was carried out using a TA Instruments Q600 SDT simultaneous DSCTGA on a powder sample of MOF and PANI@MOF composites. All samples were heated in air at a ramp rate of 25 °C/min to 1000 °C and then held isothermally at 1000 °C before ramping back down to 200 °C at 25 °C/min. A Micrometrics GEMINI 2360 was used to measure the BET surface areas of UiO-66 and UiO-66-NH_2 using N_2 at 77 K. Subsequently, BET surface area isotherms of PANI@MOF composites were collected on an Anton Paar NOVA touch. All samples were degassed at 200 °C for 3 h, and surface areas were measured using the BET equation and criteria proposed by Roquerol et al.[42,43] Scanning electron microscopy (SEM) with complimentary energy-dispersive X-ray spectroscopy (EDS) measurements were collected on a JEOL JSM-6480LV SEM and JEOL JCM-7000 SEM. The pristine UiO-66 3:1 and 2:1 PANI@UiO-66-NH_2 samples imaged were precoated using 5 nm Au nanoparticles to reduce charging, and the 3:1 PANI@UiO-66 was precoated with carbon.

Conductivity of each composite material was found using the four-point probe method, on an S-302 resistivity stand reading sheet resistivity in ohms/square in an inert N_2 atmosphere at room temperature. Eleven trials were performed on each film to achieve a statistical range of the reciprocal resistivity (sheet conductivity) for each composite. The optical electronic structure was characterized using a Persee T8DS UV/vis spectrophotometer with the IS19-1 integrating sphere attachment.

4. RESULTS AND DISCUSSION

Figure 1a,b shows FT-IR spectra of different PANI@UiO-66 and PANI@UiO-66-NH_2 composite powders. Prevalent features of the MOF spectra (black) include strong symmetric and asymmetric stretching bands from the TPA carboxylate groups at 1390 and 1584 cm^{-1} for UiO-66 and 1379 and 1565 cm^{-1} for UiO-66-NH_2. Additional peaks at 1505 cm^{-1} (UiO-66) and 1491 cm^{-1} (UiO-66-NH_2) are the result of aromatic C−C ring stretching, and the lower frequency peaks at 667 cm^{-1} (UiO-66) and 656 cm^{-1} (UiO-66-NH_2) arise from the Zr-μ-Zr stretching inside the node. There are also additional peaks due to trapped DMF solvent at 1662 cm^{-1} (UiO-66) and 1654 cm^{-1} (UiO-66-NH_2). Peaks arising singularly from UiO-66-NH_2 include the C−N aromatic amine stretch at 1252 cm^{-1} and N−H stretching at 3317 and 3444 cm^{-1}.

The IR spectrum of PANI (blue) includes characteristic N−H bending at 1468 and 1438 cm^{-1} and C−H bending at 1289 and 1230 cm^{-1}. The broad combination band coming from 1700 to 1650 cm^{-1} includes C−C ring and N−H stretches, as well as secondary N−H deformation. Combination bands before 1110 cm^{-1} include aromatic ring stretching and C−N deformation stretching.

Low doping 1:1 spectra (yellow) shows retention of all major MOF peaks at intensities comparable to the unfunctionalized MOFs; however, noticeable peaks at 1133 cm^{-1} (PANI@UiO-66) and 1140 cm^{-1} (PANI@UiO-66-NH_2) are present that do not appear in the IR spectrum of the MOFs, which can be attributed to aromatic ring stretching from the PANI functionalization. Additionally, there are shoulders on the symmetric and asymmetric COO stretching peaks arising from C−H and N−H bending in PANI. The loss of the trapped DMF solvent band at 1655 cm^{-1} is observed in the PANI@UiO-66-NH_2 composite, indicating activation of the MOF due to adsorption of aniline. This indirectly implies diffusion of aniline into MOF pores during synthesis. Additionally, hypsochromic shifting of the COO symmetric stretching peak and complimentary bathochromic shifting of the COO asymmetric peak are observed in the PANI@UiO-66 composite. These peaks are characteristics of noncovalent interactions, reducing the strain on Zr−O coordination bonds

https://dx.doi.org/10.1021/acsomega.9b03834
ACS Omega 2020, 5, 6395−6404

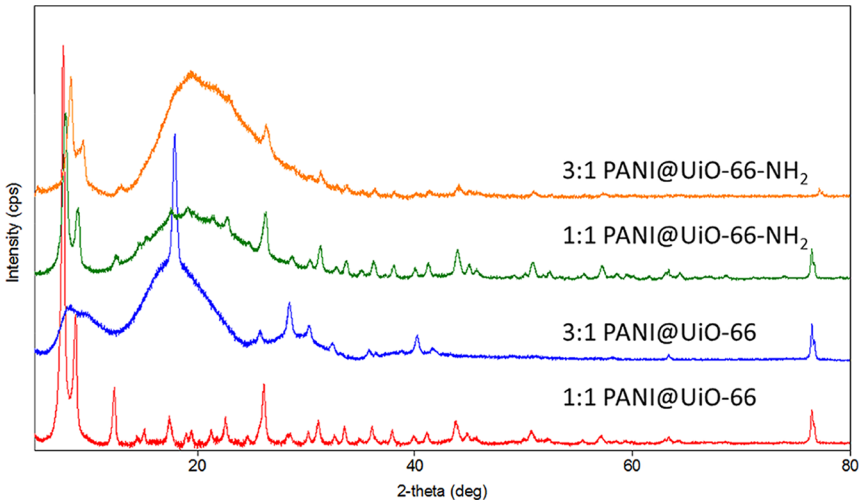

Figure 2. XRD of 1:1 and 3:1 PANI@UiO-66 and PANI@UiO-66-NH_2 composites.

as well as a general loss of ligand coordination, which is consistent with observed PXRD results (see Figure 2). Unfortunately, the broad plasmonic band created by PANI overshadows N−H stretching frequencies leaving little detail on oxidation effects on the FG.

IR spectra of higher PANI-doped composites shows overall increases in PANI stretching frequencies and broadening of spectral bands consistent with the ratio of aniline used. As expected, the PANI attributed peaks become more prominent as MOF-related peaks are reduced in intensity in the PANI@MOF composites. The spectra of PANI@UiO-66 composites show increasingly larger shifts in the COO symmetric stretching from 1:1 (1394 cm^{-1}) to 2:1 and 3:1 (1416 cm^{-1}), indicating a greater loss of Zr coordination bonding with increasing PANI concentration. In the case of PANI@UiO-66-NH_2 composites, however, retention of Zr−μ−Zr peak and symmetric O−C−O carboxylate stretching is evident in all the functionalized spectra supporting higher retention of the MOF motif in solution. This supports the hypothesis that PANI chain growth is restricted by the secondary mechanistic pathway provided by the amine functionalization of the MOF linker. This retention of fixed MOF symmetric carboxylate stretching is further supported by PXRD results (Figure 2), indicating that the UiO-66-NH_2 has much higher resistance to structural collapse in the strong oxidative environment. This is likely due to the greater decentralization of electron density provided from the ATPA ligand used in UiO-66-NH_2. The lone electron pairs of the aliphatic amine groups provide a sterically more favorable site for oxidation than the carboxylate coordination bonds. Thus, this amine group behaves as a terminal site for oxidative polymerization of PANI ligands while also acting as a protecting group for the MOF coordination bond.

PXRD data confirmed that the UiO-66 MOF was successfully synthesized and that the structure is stable and retains its crystal structure in both the PANI@UiO-66 and PANI@UiO-66-NH_2 composites.[14] As X-ray scattering increases with Z, the diffraction pattern is dominated by the inorganic portion of the MOF, and it is not possible to discern information about light atoms; therefore, only Zr positions can be modelled accurately. The peak positions matched the reported structure for UiO-66[14] with the 1:1 PANI@UiO-66 showing a high degree of crystallinity. This crystallinity was largely preserved in the 1:1 PANI@UiO-66-NH_2 with a higher background and some peak broadening accompanying the introduction of the ATPA linker indicating a stronger interaction with the amorphous PANI. The UiO-66 peaks are still distinguishable in samples with higher PANI (3:1 pictured) concentration but show significant background and broadening, with the lower intensity peaks lost in the increased noise from the higher proportion of the amorphous material in these composites. This is especially true for the 3:1 PANI@UiO-66 composite in which fewer of the weaker UiO-66 MOF peaks are discernible yet shows a marked increase in intensity for the peak at 2θ = 17.83(1)°, accompanied by additional peaks at 2θ = 28.50(2)° and 30.3(3)°, which are not observed in the 3:1 composite of UiO-66-NH_2. These three peaks may indicate some degradation of the UiO-66 MOF to another Zr-containing phase such as the baddeleyite polymorph of ZrO_2 (PDF card 01-083-0944, CSD ICSD 80050). Both UiO-66 and baddeleyite phases have a peak around $2\theta \approx 18°$, so the relatively high intensity of the peak in this region may indicate it is a composite arising from both phases. This breakdown of MOF is furthermore evidenced by the extreme drop in the surface area and thermal stability of the material in the 3:1 PANI@UiO-66 composite.

Refinement of the lattice parameters using the Rietveld method showed a slight expansion in the lattice parameter with introduction of the ATPA linker as shown in Table 1. The 3:1 PANI@UiO-66, however, does not show this increase in the lattice constant upon increasing PANI concentration. This expansion in the lattice parameter is likely due to greater synergy between the PANI polymer and organic linker of UiO-66-NH_2. The PANI polymer is capable of covalent linkage to the linker of UiO-66-NH_2 through the −NH_2 group of ATPA,

Table 1. Lattice Parameters of Different PANI@MOF Composites

composite sample	lattice parameter (Å)
1:1 PANI@UiO-66	20.650(3)
1:1 PANI@UiO-66-NH_2	20.69(2)
3:1 PANI@UiO-66	20.648(6)
3:1 PANI@UiO-66-NH_2	20.72(2)

https://dx.doi.org/10.1021/acsomega.9b03834
ACS Omega 2020, 5, 6395−6404

whereas the UiO-66 MOF likely interacts with the PANI polymer through noncovalent interactions.

Surface area measurements of pristine UiO-66 and UiO-66-NH_2 fall well within range reported in literature for these materials (Table S9) indicating activation of MOF before PANI functinalization.[15,27,28] BET isotherms of composite materials show a decreasing surface area with an increasing PANI content as expected for composite systems. The hysteresis loops of each sample (Figure S16) also reflect the composite nature of the PANI-functionalized MOFs.[44] Interestingly, the PANI@UiO-66-NH_2 composites retain higher surface areas than the PANI@UiO-66 materials, with 3:1 PANI@UiO-66 exhibiting a near complete loss of all nanoporosity (Table 2). This correlates well with FT-IR and PXRD data suggesting lower retentions of the pristine MOF content in the UiO-66 composites and further supports the higher chemical stability of UiO-66-NH_2 discussed previously.

Table 2. BET Surface Area and Sheet Conductivity Measurements of PANI@MOF Composites

material	BET SA (m^2/g)	wt % MOF	average sheet conductivity (mS/sq.)
1:1 PANI@UiO-66-NH_2	815	68%	0.019
1:1 PANI@UiO-66	234	19%	0.23
3:1 PANI@UiO-66-NH_2	331	26%	0.85
3:1 PANI@UiO-66	36	3%	3.04

Furthermore, surface area analysis can be used as a direct reflection of the pristine MOF content in composite systems assuming that all nanoporosity is attributed purely to the MOF in the material, as reflected by SEM imaging. This method of the estimating pristine MOF content was demonstrated by Bunge et al. and is based on eq 1 below.[41]

$$\frac{\text{polymer@MOF area } (m^2)}{\text{polymer@MOF total mass (g)}} = (\text{wt\% of pristine MOF}) \times \left(\text{pristine MOF surface area}\left(\frac{m^2}{g}\right)\right) \quad (1)$$

The relative weight percent (wt %) of pristine MOF (Table 2) in each composite reflects the preservation of crystalline MOF in the sample, but it serves more as a relative estimation than definitive elemental analysis. These values are likely an underestimation of the true MOF content, as the SEM-EDS analysis and PXRD analysis suggest that PANI nanofibers can block MOF pore sights and polymer oxidation leads to degraded MOFs with lower surface areas in general. Comparison of the relative wt % of the composites, however, does show that PANI@UiO-66-NH_2 better preserves pristine MOF compared to PANI@UiO-66, as evidenced by the large discrepancy in the surface area between 1:1 and 3:1 PANI-functionalized MOFs.

Results from TGA (Figure 3) of PANI@UiO-66 and PANI@UiO-66-NH_2 show characteristic degradation steps for each MOF respectfully beginning with solvent evaporation from 50 to 100 °C. The amine-functionalized MOF, UiO-66-NH_2 shows a gradual degradation step from 300 to 600 °C, whereas the UiO-66 MOF shows a more pronounced degradation step at 500−550 °C. This difference is due to inductive effects caused by the electronegative amine functional group of UiO-66-NH_2, which causes the MOF to be less thermally stable than UiO-66.[27,28] Beyond 500−600 °C, all MOF crystallinity lost as the MOF breaks down into tetragonal zirconia.[32] The degradation of PANI is observed in three steps reported for Cl-doped emeraldine salt: solvent evaporation

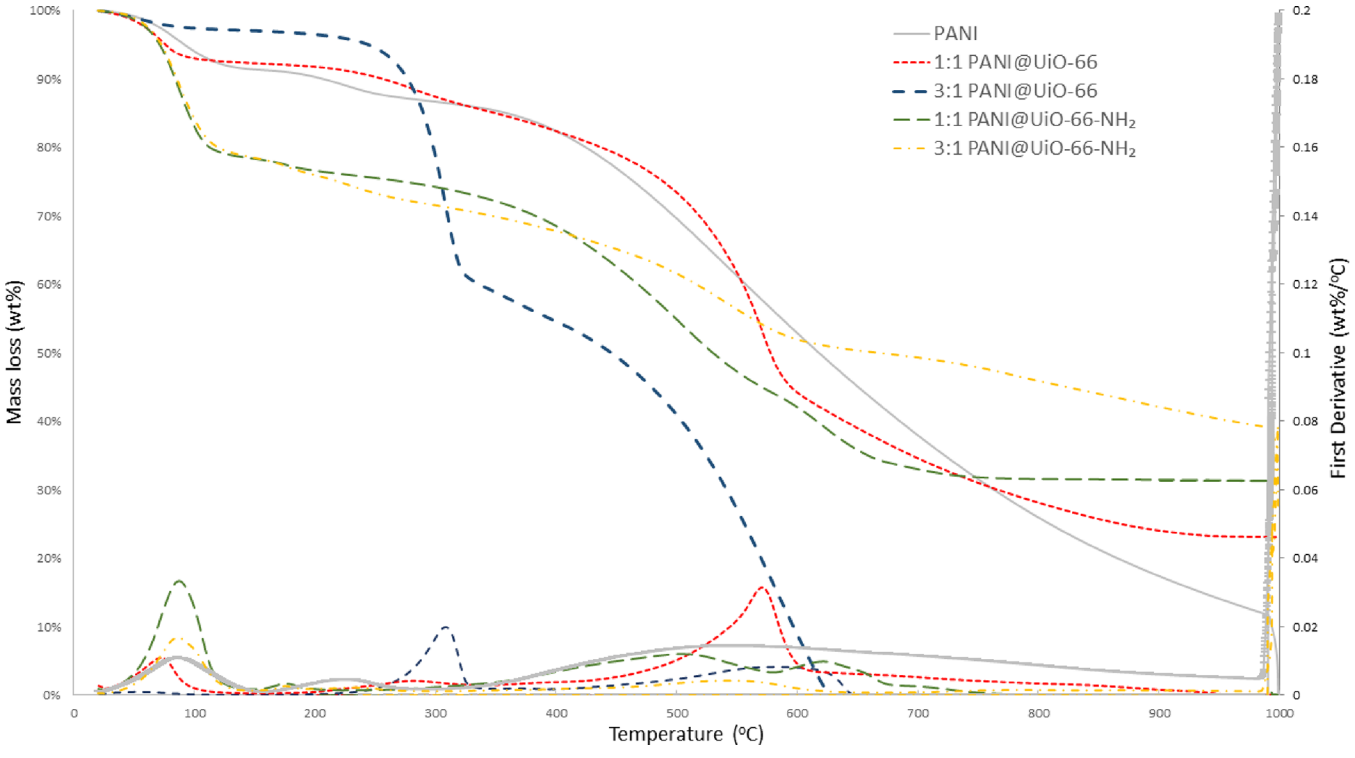

Figure 3. TGA of PANI@UiO-66 and PANI@UiO-66-NH_2 composites for low doping (1:1) and high doping (3:1) PANI@MOF Composites

https://dx.doi.org/10.1021/acsomega.9b03834
ACS Omega 2020, 5, 6395−6404

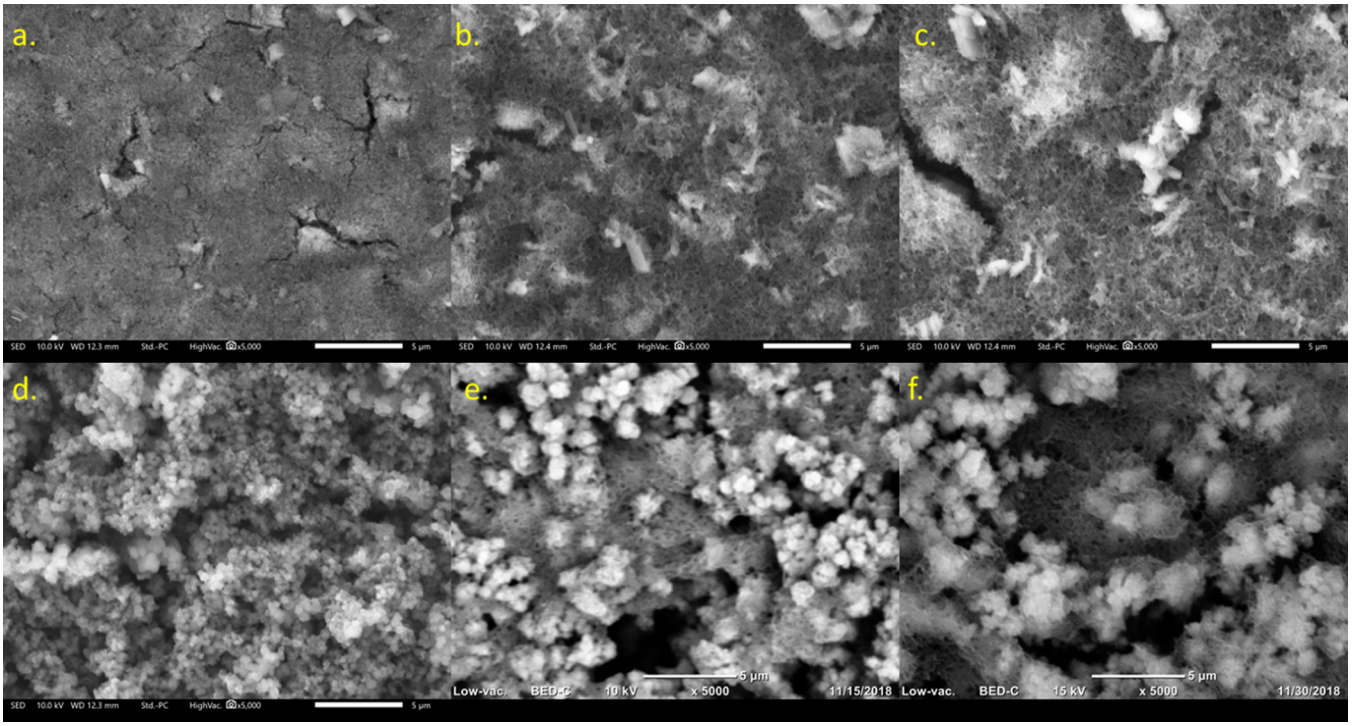

Figure 4. SEM images of PANI@UIO-66 at PANI/MOF ratios of 1:1 (A), 2:1 (B), and 3:1 (C), and PANI@UiO-66-NH_2 at PANI:MOF ratios of 1:1 (D), 2:1 (E), and 3:1 (F).

from 50 to 100 °C followed by protonic acid decomposition from 160 to 275 °C and finally the breakdown of the polymer chain gradually into small molecules, such as ammonia and aniline, from 350 to 1000 °C.[33,34] All MOFs excluding 3:1 PANI@UiO-66 exhibit this broad degradation of the polymer up to 1000 °C.

In the 3:1 PANI@UiO-66 composite, MOF degradation steps are still shown, but the partial framework collapse has clearly resulted in losses of thermal stability. Interestingly, a new degradation step appears at 310 °C accounting for 35% degradation. This is attributed to the breakdown of the polymorphous material into base reagents, aniline, and zirconium chloride. This can be further evidenced by the TGA of 1:1 PANI@UiO-66, which also has a much smaller inflection point in this region not observed in any other material. The 3:1 composite also shows complete degradation at 600 °C indicating the polymorph formation also results in less thermally robust PANI.

Conversely, the amine-functionalized composites exhibit all major steps associated with each material. Interestingly, the 1:1 composite also features a sharp degradation step from 585 to 675 C, which may be attributed to the fragments of polymer attached to MOF side chains. This observed retention of major degradation steps and proposed polymer breakdown step coincides with the PXRD and FT-IR results, which clearly demonstrate penetration of PANI into the MOF network and covalent linkage to UiO-66-NH_2 that is not observed for UiO-66.

Samples imaged using SEM were prepped via drop deposition (1 mg/cm^2) on atomically flat Mica discs. All composites were conductively coated with gold or carbon and imaged using backscatter electron detection to reduce charging and increase resolution. EDS was performed prior to conductive coatings. Further, images (Figure S9) of pure PANI show a porous nanofiber network (85−900 nm diameter) congruent with the synthesis reported in literature.[25] EDS analysis confirms a fully homogeneous PANI network in all cases with negligible precursor salt contamination. The UiO-66 and UiO-66-NH_2 MOF maintains a powder form giving an octahedral morphology and shows substantially larger aggregates of 400−1000 nm in size (Figures S10 and S11). This is consistent with PXRD data and MOF topologies reported in the literature.[1,37,38]

Because the composites are bulk phase, low magnification of composite films provides a great deal of information regarding surface morphology and aniline polymerizations in the presence of the MOF. In all EDS spectral maps (see the Supporting Information section), the PANI is uniform and the MOF aggregates do not appear to be isolated but rather spread uniformly throughout. This contrasts the topology shown in the images, which is likely the result of the electron beam penetrating into MOF aggregates embedded beneath the PANI network. Although reasonable for semiquantitative analysis, Zr peaks from EDS analysis could not be isolated to the visible MOF aggregate sites in the SEM images.

The composite film in low doping (1:1) PANI@UiO-66 is fully aggregated, and the PANI nanofiber network cannot be observed (Figure 4a). This film, thus, is mostly aggregated UiO-66, which is supported by PXRD results showing peaks consistent with the pristine MOF. The lack of any surface detail suggests that the PANI network aggregates between MOF particles. This behavior was not observed in other papers using polyaniline/MOF composites that reported a core−shell relationship.[26,35,36] Counterintuitively, the 1:1 PANI@UiO-66-NH_2 shows high retention of single-MOF particles with a visible PANI network beneath (Figure 4d). The network is too aggregated to show visible branching, but the core−shell relationship reported is more plausible in this case, considering composite film morphology has not significantly changed from pure UiO-66-NH_2. This reasoning is supported by PXRD

https://dx.doi.org/10.1021/acsomega.9b03834
ACS Omega 2020, 5, 6395−6404

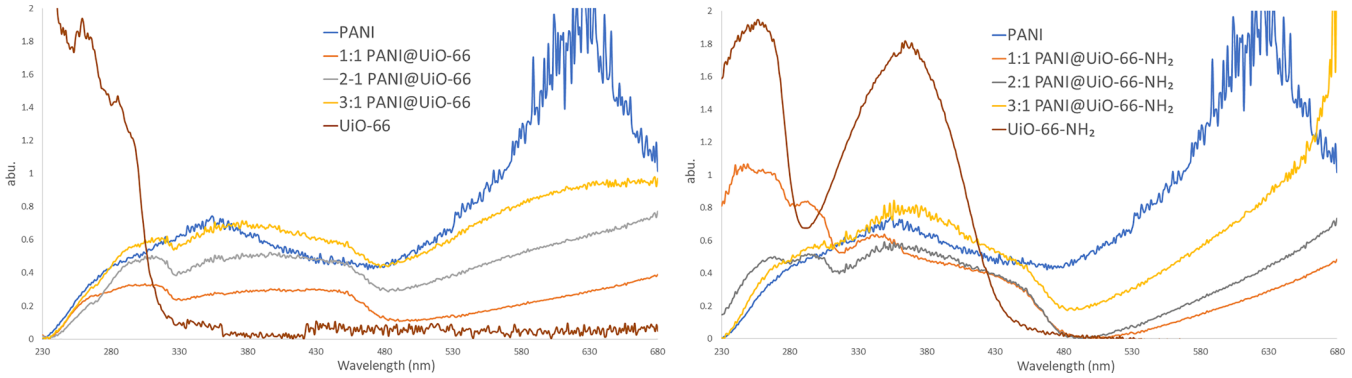

Figure 5. UV−vis spectra of PANI@UiO-66 composites (left) and PANI@UiO-66-NH_2 composites (right).

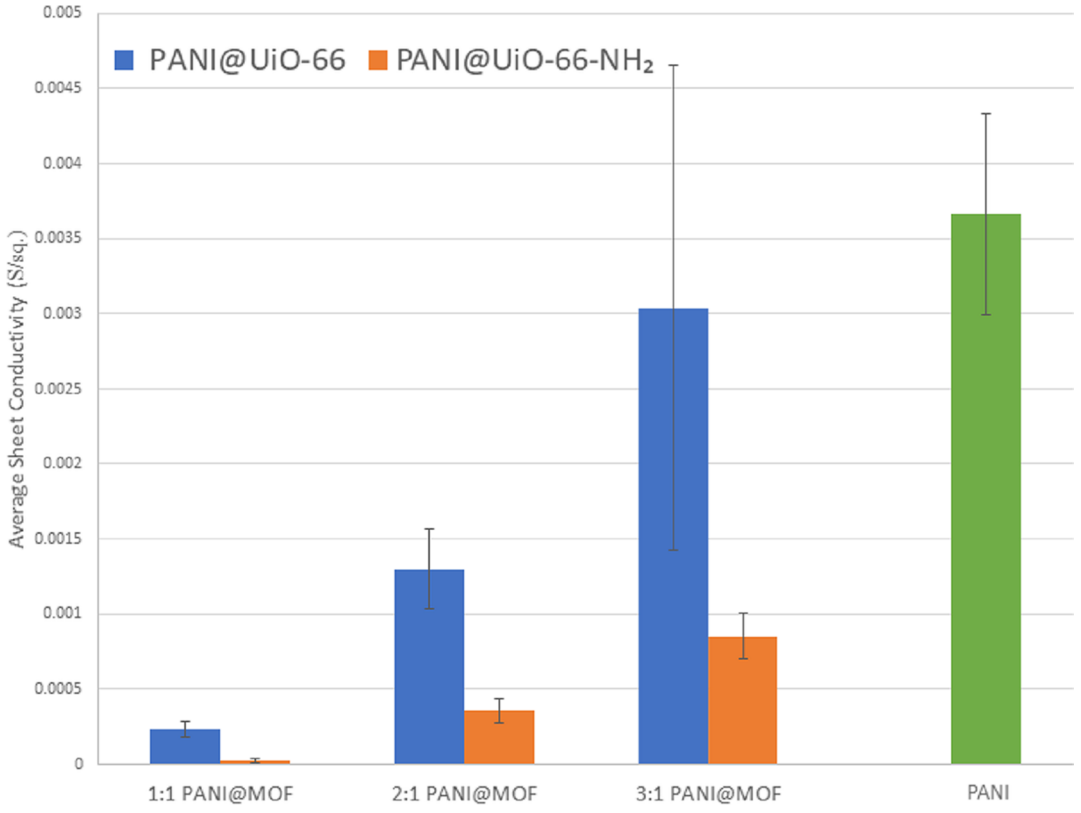

Figure 6. Average sheet conductivity of all polymer-MOF hybrid composites and PANI in S/sq.

result showing that increasing the relative amount of PANI polymer present significantly alters spectral peaks and peak intensity. However, large amounts of carbon and oxygen can clearly be seen in greater quantity around large MOF aggregate sites in the EDS spectra, which could be attributed to greater MOF/PANI cohesion. Additionally, the EDS spectra also show more PANI being formed in the PANI@UiO-66 composites over the PANI@UiO-66-NH_2 composites, which supports the notion that polymerization off the NH_2 group of the organic linker inhibits orderly polymer stacking of PANI. In the amine-functionalized spectra, the MOF ligands participate in oxidative polymerization on its surface leading to this greater cohesion, which can be visualized in high doping 2:1 and 3:1 PANI@UiO-66-NH_2 SEM images (Figure 4e,f).

SEM images of the high doping UiO-66 and UiO-66-NH_2 composites show amorphous PANI fibral networks around aggregated MOF crystals. MOF aggregates are more spaced throughout the material in each image, but the PANI network appears to be more prevalent in the PANI@UiO-66 composites. This is supported by EDS results showing that more PANI has formed in the unfunctionalized composites. The MOF crystal structure, however, appears different in the 2:1 and 3:1 PANI@UiO-66 composites, adopting larger needle-like crystal forms. This is likely due to some degradation of the UiO-66 framework to another Zr-containing phase, which is consistent with the PXRD results of the 3:1 PANI@UiO-66 composite. The PXRD spectrum (Figure 2) shows broadening due to the amorphous PANI network, which makes it difficult to observe all peaks that could arise from the UiO-66 MOF; however, there is a strong increase in intensity for the peak at $2\theta = 17.83(1)°$, suggesting that a baddeleyite polymorph of ZrO_2 has formed within the composite. This decomposition is not observed in the SEM images, TGA, or PXRD spectra of the PANI@UiO-66-NH_2

https://dx.doi.org/10.1021/acsomega.9b03834
ACS Omega 2020, 5, 6395−6404

composites. As indicated previously, the amine-functionalized linker shows greater chemical resistance, which allows the UiO-66-NH_2 to retain its structure in the presence of a strong oxidant, whereas UiO-66 does not.

In the higher magnification image of the 3:1 PANI@UiO-66-NH_2 (Figure S8), the PANI nanofibers are observed more clearly branching out of MOF aggregates. Comparing this finding with the PXRD results and 1:1 PANI@UiO-66-NH_2 image, it can be concluded that PANI nanofibers are covalently linked to the MOF surface, as the MOF core clearly encompasses a PANI network over the entire surface (Figure 5).

Studies on optoelectronic and conducting properties of all PANI@MOF composite materials reveal a great deal of information on how PANI conduction can be tuned by the synthesis of nanofibers around MOF architectures. As seen in Figure 5, the PANI network adds a slight photosensitization to MOF with a 2.5 eV bandgap. In addition, the plasmonic band absorption due to the PANI network past 530 nm provides unique conducting capabilities to the material.[25,29] This is relevant in the design of conductive composite MOF materials containing Zr-based MOFs, which are mostly insulating by nature. The UiO-66 MOF, in particular, is considered quasisemiconducting with a 4.0 eV bandgap (BG); there is a slight bathochromic shift of the UiO-66 BG to 3.8 eV observed upon PANI functionalization. This is attributed to defects in the MOF structure introduced during the synthesis of PANI nanofibers, which partially decomposes the UiO-66 framework.[30] The amine functionality in turn shifts the MOF bandgap to 2.9 eV. Under oxidative polymerization conditions, partial oxidation of the amine group from TPA results in a new peak at 336 nm observed in the 1:1 and 2:1 spectra. Minimal shifting in PANI absorption bands and overlap with MOF transitions is observed in 1:1, 2:1, and 3:1 composites.

Sheet conductivity was measured using a four-point probe in an inert atmosphere to provide information on both the concentration of dopant (PANI) and the effects of using different linkers. The conducting mechanism of PANI itself has been studied extensively, and it has been shown that PANI is composed of conducting emeraldine salt grains and insulating emeraldine base grains.[31] When the grains π stack in one dimension, conducting grains can perpetuate charge across the film more efficiently. The results shown in Figure 6 indicate that the insulating UiO-66 aggregate particles in the composite block PANI fiber formation resulting in an increase in sheet resistivity. However, as PANI concentration increases and the MOF aggregates begin to decompose the PANI can readily stack conducting grains around the needle like crystals observed in the PANI@UiO-66 composites. This greater heterogeneity and high conductivity results in larger variability observed in the 3:1 PANI@UiO-66 composite electrode.

The same concentration effect on conduction is seen in the PANI@UiO-66-NH_2 composites, but these materials ultimately possess much less mobile charge carriers than the PANI@UiO-66 composites. As previously shown, the UiO-66-NH_2 MOF is more resistant to structural collapse during oxidation and hydrothermal conditions, allowing for better synergy between the UiO-66-NH_2 framework and the PANI polymer chains ultimately resulting in higher relative surface areas (Table 2). This causes nanofiber formation to be sterically hindered by small MOF pores and directed linearly in all directions from MOF surface and ultimately leads to poor film integrity, as evidenced by holes observed in SEM images and less developed PANI network. The amine sites in the MOF also act as a competing reductant for APS, which may result in lower PANI yields despite providing surface site covalency. Ultimately, the greater synergy and chemical stability of the PANI@UiO-66-NH_2 composites come at the cost of low concentration of conduction grains and bulk film stability.

5. CONCLUSIONS

The effects of aniline concentration, oxidant exposure, and linker functionality on structural and electronic properties of PANI@UiO-66 and PANI@UiO-66-NH_2 polymer-MOF hybrid composites were thoroughly investigated. The PANI@MOF composites all display tunable semiconducting behavior dependent on linker functionality and aniline concentration during postsynthetic modification. The amine-functionalized MOF shows higher chemical resilience to synthetic conditions for aniline polymerization and ultimately greater cohesion with PANI nanofibers. Conductivity measurements revealed a direct relationship between aniline concentration and conduction. The greater synergy of the PANI@UiO-66-NH_2 composites ultimately led to constrained fiber formation and lower conductivity, but the MOF motif was retained after modification. The UiO-66 MOF, however, is embedded noncovalently within the PANI polymer network resulting in higher conductivities for PANI@UiO-66 composites but at the cost of MOF structural stability.

■ ASSOCIATED CONTENT

Supporting Information

The Supporting Information is available free of charge at https://pubs.acs.org/doi/10.1021/acsomega.9b03834.

EDS spectra and elemental analyses of all materials synthesized in manuscript along with a higher magnification SEM image of 3:1 PANI@UiO-66-NH_2 composite, SEM, PXRD, and band gap measurements with tables, and N_2 adsorption isotherms and surface areas of all base materials: PANI, UiO-66 and UiO-66-NH_2 (PDF)

■ AUTHOR INFORMATION

Corresponding Author

Daniel S. Kissel − *Department of Chemistry, Lewis University, Romeoville, Illinois 60446, United States;* orcid.org/0000-0003-1779-8488; Phone: (815) 588-7435; Email: kisselda@lewisu.edu

Authors

Jordan Shanahan − *Department of Chemistry, Lewis University, Romeoville, Illinois 60446, United States*

Eirin Sullivan − *Department of Chemistry, Illinois State University, Normal, Illinois 61761, United States*

Complete contact information is available at: https://pubs.acs.org/10.1021/acsomega.9b03834

Author Contributions

[§]Jordan Shanahan, Eirin Sullivan and Daniel Kissel contributed equally. The manuscript was written through contributions of all authors. All authors have given approval to the final version of the manuscript.

Notes

The authors declare no competing financial interest.

https://dx.doi.org/10.1021/acsomega.9b03834
ACS Omega 2020, 5, 6395−6404

■ ACKNOWLEDGMENTS

Funding for this work was supported by the Lasallian Research Grant and Caterpillar Scholar Award from Lewis University, and the Illinois State Department of Chemistry and College of Arts and Sciences. The authors would also like to acknowledge McCrone Group, Inc. for providing access to their SEM-EDS instruments for the images reported in this work, and Anton Paar USA, Inc. for help with the BET isotherm measurements.

■ REFERENCES

(1) Abid, H. R.; Shang, J.; Ang, H. M.; Wang, S. Amino-functionalized Zr-MOF nanoparticles for adsorption of CO_2 and CH_4. *Int J Smart Nano Mater.* **2013**, *4*, 72−82.
(2) Poloni, R.; Kim, J. Thermodynamics of gas adsorption in MOFs using Ab Initio calculations. *Int. J. Quantum Chem.* **2016**, *116*, 569−572.
(3) Tan, L.; Li, H.; Zhou, Y.; Zhang, Y.; Feng, X.; Wang, B.; Yang, Y.-W. Zn^{2+}-Triggered Drug Release from Biocompatible Zirconium MOFs Equipped with Supramolecular Gates. *Small* **2015**, *11*, 3807−3813.
(4) Xiao, J.-D.; Jiang, H.-L. Metal−Organic Frameworks for Photocatalysis and Photothermal Catalysis. *Acc. Chem. Res.* **2019**, *52*, 356−366.
(5) Chen, Y. F.; Tan, L. L.; Liu, J. M.; Qin, S.; Xie, Z. Q.; Huang, J. F.; Xu, Y. W.; Xiao, L. M.; Su, C. Y. Calix[4]arene based dye-sensitized Pt@UiO-66-NH_2 metal-organic framework for efficient v. *Appl Catal B Environ.* **2017**, *206*, 426−433.
(6) Nasalevich, M. A.; Goesten, M. G.; Savenije, T. J.; Kapteijn, F.; Gascon, J. Enhancing optical absorption of metal-organic frameworks for improved visible light photocatalysis. *Chem Commun.* **2013**, *49*, 10575−10577.
(7) Nasalevich, M. A.; Hendon, C. H.; Santaclara, J. G.; Svane, K.; van der Linden, B.; Veber, S. L.; Fedin, M. V.; Houtepen, A. J.; van der Veen, M. A.; Kapteijn, F.; Walsh, A.; Gascon, J. Electronic origins of photocatalytic activity in d^0 metal organic frameworks. *Sci. Rep.* **2016**, *6*, 23676.
(8) Prasad, R. L.; Kushwaha, A. Synthesis, characterization, and solid state electrical conductivity of coordination polymers with copper and zinc. *J. Coord. Chem.* **2012**, *65*, 4230−4244.
(9) Sheberla, D.; Bachman, J. C.; Elias, J. S.; Sun, C.-J.; Shao-horn, Y.; Dincă, M. Conductive MOF electrodes for stable supercapacitors with high areal capacitance. *Nat. Mater.* **2017**, *16*, 220−224.
(10) Han, S.; Warren, S. C.; Yoon, S. M.; Malliakas, C. D.; Hou, X.; Wei, Y.; Kanatzidis, M. G.; Grzybowski, B. A. Tunneling Electrical Connection to the Interior of Metal-Organic Frameworks. *J. Am. Chem. Soc.* **2015**, *137*, 8169−8175.
(11) Yuan, S.; Qin, J.-S.; Lollar, C. T.; Zhou, H.-C. Stable Metal-Organic Frameworks with Group 4 Metals: Current Status and Trends. *ACS Cent. Sci.* **2018**, *4*, 440−450.
(12) Hu, Z.; Zhao, D. De facto methodologies toward the synthesis and scale-up production of UiO-66-type metal organic frameworks and membrane materials. *Dalton Trans.* **2015**, *44*, 19018−19040.
(13) Kim, M.; Cohen, S. M. Discovery, development, and functionalization of Zr(IV)-based metal−organic frameworks. *CrystEngComm* **2012**, *14*, 4096−4104.
(14) Cavka, J. H.; Jakobsen, S.; Olsbye, U.; Guillou, N.; Lamberti, C.; Bordiga, S.; Lillerud, K. P. A New Zirconium Inorganic Building Brick Forming Metal Organic Frameworks with Exceptional Stability. *J. Am. Chem. Soc.* **2008**, *130*, 13850−13851.
(15) Valenzano, L.; Civalleri, B.; Chavan, S.; Bordiga, S.; Nilsen, M. H.; Jakobsen, S.; Lillerud, K. P.; Lamberti, C. Disclosing the complex structure of UiO-66 metal organic framework: A synergic combination of experiment and theory. *Chem. Mater.* **2011**, *23*, 1700−1718.
(16) Jin, Z.; Yang, H. Exploration of Zr−Metal−Organic Framework as Efficient Photocatalyst for Hydrogen Production. *Nanoscale Res. Lett.* **2017**, *12*, 539.
(17) Wang, W.; Xu, X.; Zhou, W.; Shao, Z. Recent Progress in Metal-Organic Frameworks for Applications in Electrocatalytic and Photocatalytic Water Splitting. *Adv Sci.* **2017**, *4*, 1600371.
(18) Musho, T.; Li, J.; Wu, N. Band Gap Modulation of Functionalized Metal-Organic Frameworks. *Phys. Chem. Chem. Phys.* **2014**, *16*, 23646−23653.
(19) Shen, L.; Liang, R.; Luo, M.; Jing, F.; Wu, L. Electronic effects of ligand substitution on metal−organic framework photocatalysts: the case study of UiO-66. *Phys. Chem. Chem. Phys.* **2015**, *17*, 117−121.
(20) Ćirić-Marjanović, G. Recent advances in polyaniline research: Polymerization mechanisms, structural aspects, properties and applications. *Synth. Met.* **2013**, *177*, 1−47.
(21) Navarchian, A. H.; Hasanzadeh, Z.; Joulazadeh, M. Effect of polymerization conditions on reaction yield, conductivity, and ammonia sensing of polyaniline. *Adv. Polym. Technol.* **2013**, *32*, 5−9.
(22) Boeva, Z. A.; Sergeyev, V. G. Polyaniline: Synthesis, properties, and application. *Polym Sci Ser C.* **2014**, *56*, 144−153.
(23) Kandiah, M.; Usseglio, S.; Svelle, S.; Olsbye, U.; Lillerud, K. P.; Tilset, M. Post-synthetic modification of the metal−organic framework compound UiO-66. *J. Mater. Chem.* **2010**, *20*, 9848.
(24) Marshall, R. J.; Forgan, R. S. Postsynthetic Modification of Zirconium Metal-Organic Frameworks. *Eur. J. Inorg. Chem.* **2016**, *2016*, 4310−4331.
(25) Li, D.; Kaner, R. B. Shape and Aggregation Control of Nanoparticles: Not Shaken, Not Stirred. *J. Am. Chem. Soc.* **2006**, *128*, 968−975.
(26) Wang, W.; Wang, L.; Li, Y.; Liu, S.; Xie, Z.; Jing, X. Nanoscale Polymer Metal−Organic Framework Hybrids for Effective Photothermal Therapy of Colon Cancers. *Adv. Mater.* **2016**, *28*, 9320−9325.
(27) Shearer, G. C.; Chavan, S.; Ethiraj, J.; Vitillo, J. G.; Svelle, S.; Olsbye, U.; Lamberti, C.; Bordiga, S.; Lillerud, K. P. Tuned to perfection: Ironing out the defects in metal-organic framework UiO-66. *Chem. Mater.* **2014**, *26*, 4068−4071.
(28) Luu, C. L.; Van Nguyen, T. T.; Nguyen, T.; Hoang, T. C. Synthesis, characterization and adsorption ability of UiO-66-NH_2. *Adv Nat Sci Nanosci Nanotechnol.* **2015**, *6*, No. 025004.
(29) Osorio-Fuente, J. E.; Gómez-Yáñez, C.; de los Ángeles Hernández-Pérez, M.; Pérez-Moreno, F. Camphor Sulfonic Acid-hydrochloric acid codoped polyaniline/polyvinyl alcohol composite: Synthesis and characterization. *J Mex Chem Soc* **2014**, *58*, 52−58.
(30) De Vos, A.; Hendrickx, K.; Van Der Voort, P.; Van Speybroeck, V.; Lejaeghere, K. Missing Linkers: An Alternative Pathway to UiO-66 Electronic Structure Engineering. *Chem. Mater.* **2017**, *29*, 3006−3019.
(31) Lin, Y. F.; Chen, C. H.; Xie, W. J.; Yang, S. H.; Hsu, C. S.; Lin, M. T.; Jian, W. B. Nano approach investigation of the conduction mechanism in polyaniline nanofibers. *ACS Nano* **2011**, *5*, 1541−1548.
(32) Kandiah, M.; Nilsen, M. H.; Usseglio, S.; Jakobsen, S.; Olsbye, U.; Tilset, M.; Larabi, C.; Quadrelli, E. A.; Bonino, F.; Lillerud, K. P. Synthesis and Stability of Tagged UiO-66 Zr-MOFs. *Chem. Mater.* **2010**, 6632−6640.
(33) Ansari, R.; Price, W. E.; Wallace, G. G. Effect of thermal treatment on the electroactivity of polyaniline. *Polymer* **1996**, *37*, 917−923.
(34) Cardoso, M. J. R.; Lima, M. S. F.; Lenz, D. M. Polyaniline synthesized with functionalized sulfonic acids for blends manufacture. *Mat. Res.* **2007**, *10*, 425−429.
(35) Wang, Y.; Wang, L.; Huang, W.; Zhang, T.; Hu, X.; Perman, J. A.; Ma, S. A metal−organic framework and conducting polymer based electrochemical sensor for high performance cadmium ion detection. *J. Mater. Chem. A* **2017**, *5*, 8385.
(36) Shao, L.; Wang, Q.; Ma, Z.; Ji, Z.; Wang, X.; Song, D.; Liu, Y.; Wang, N. A high-capacitance flexible solid-state supercapacitor based on polyaniline and Metal-Organic Framework (UiO-66) composites. *J. Power Sources* **2018**, *379*, 350−361.
(37) Ma, L.; He, Y.; Wang, Y.; Wang, Y.; Li, R.; Huang, Z.; Jiang, Y.; Gao, J. Nanocomposites of Pt nanoparticles anchored on UiO66-NH_2 as carriers to construct acetylcholinesterase biosensors for organo-

https://dx.doi.org/10.1021/acsomega.9b03834
ACS Omega 2020, 5, 6395−6404

phosphorus pesticide detection. *Electrochim. Acta* **2019**, *318*, 525−533.
(38) Zhou, J. J.; Wang, R.; Liu, X. L.; Peng, F. M.; Li, C. H.; Teng, F.; Yuan, Y. P. In situ growth of CdS nanoparticles on UiO-66 metal-organic framework octahedrons for enhanced photocatalytic hydrogen production under visible light irradiation. *Appl. Surf. Sci.* **2015**, *346*, 278−283.
(39) Singh, A. K.; Gonuguntla, S.; Mahajan, B.; Pal, U. Noble metal-free integrated UiO-66-PANI-Co_3O_4catalyst for visible-light-induced H_2production. *Chem Commun.* **2019**, *55*, 14494−14497.
(40) Zhang, C.; Tian, J.; Rao, W.; Guo, B.; Fan, L.; Xu, W.; Xu, J. Polypyrrole@metal-organic framework (UIO-66)@cotton fabric electrodes for flexible supercapacitors. *Cellulose* **2019**, *26*, 3387−3399.
(41) Bunge, M. A.; Davis, A. B.; West, K. N.; West, C. W.; Glover, T. G. Synthesis and Characterization of UiO-66-NH_2Metal-Organic Framework Cotton Composite Textiles. *Ind. Eng. Chem. Res.* **2018**, *57*, 9151−9161.
(42) Rouquerol, J., Rouquerol, F., Llewellyn, P., Maurin, G., Sing, K. S.. *Adsorption by Powders and Porous Solids: Principles, Methodology and Applications*; Academic Press: London, 2013.
(43) Howarth, A. J.; Peters, A. W.; Vermeulen, N. A.; Wang, T. C.; Hupp, J. T.; Farha, O. K. Best practices for the synthesis, activation, and characterization of metal−organic frameworks. *Chem. Mater.* **2016**, *29*, 26−39.
(44) Sing, K. S. W.; Williams, R. T. Physisorption hysteresis loops and the characterization of nanoporous materials. *Adsorpt Sci Technol.* **2016**, *22*, 773−782.

https://dx.doi.org/10.1021/acsomega.9b03834
ACS Omega 2020, 5, 6395−6404